# An efficient three-dimensional solid finite element dynamic analysis of reinforced concrete structures

## K. V. Spiliopoulos[*,†,‡] and G. Ch. Lykidis[§,¶]

*Department of Civil Engineering, Institute of Structural Analysis and Aseismic Research,*
*National Technical University of Athens, Zografou Campus, Zografou 157-73, Athens, Greece*

## SUMMARY

Most of the finite element analyses of reinforced concrete structures are restricted to two-dimensional elements. Three-dimensional solid elements have rarely been used although nearly all reinforced concrete structures are under a triaxial stress state. In this work, a three-dimensional solid element based on a smeared fixed crack model that has been used in the past mainly for monotonic static loading analysis is extended to cater for dynamic analysis. The only material parameter that needs to be input for this model is the uniaxial compressive strength of concrete. Steel bars are modelled as uniaxial elements and an embedded formulation allows them to have any orientation inside the concrete elements. The proposed strategy for loading or unloading renders a numerical procedure which is stable and efficient. The whole process is applied to two RC frames and compared against existing experiments in the literature. Results show that the proposed approach may adequately be used to predict the dynamic response of a structure. Copyright © 2005 John Wiley & Sons, Ltd.

KEY WORDS:  dynamic analysis; non-linear RC analysis; smeared crack model; 3D solid finite element; seismic loading; RC concrete frames

## 1. INTRODUCTION

The finite element non-linear analysis of reinforced concrete (RC) structures under dynamic loading can be a powerful tool for predicting their behaviour in order to evaluate the safety levels of design. To get an overall estimation, especially for framed structures, one may use approaches based on either concentrated plasticity methods (plastic hinges) or distributed plasticity ones (fibre models). Nevertheless, for a more realistic prediction any structure should

---

*Correspondence to: K. V. Spiliopoulos, Department of Civil Engineering, Institute of Structural Analysis and Aseismic Research, National Technical University of Athens, Zografou Campus, Zografou 157-73, Athens, Greece.
†E-mail: kvspilio@central.ntua.gr
‡Associate Professor.
§E-mail: glykid@mail.ntua.gr
¶PhD candidate.

Copyright © 2005 John Wiley & Sons, Ltd.

be considered as three dimensional, and therefore triaxial stress–strain behaviour is more appropriate.

Smeared cracking is the most widely used way to describe the cracking processes in concrete structures modelled by finite elements. The description of cracking in concrete is done within the framework of damage mechanics. The fixed crack model assumes that when a crack forms normal to the maximum principal tensile stress its orientation remains fixed throughout the analysis [1]. Another approach that assumes rotation of crack orientation due to residual tensile stress if concrete is considered as quasi-brittle is the rotating crack model [2, 3]. The more sophisticated microplane model assumes that the material is characterized by a relation between stress and strain components on planes of various orientations. One of its latest versions [4, 5] uses four material parameters which, however, increase the computational cost considerably [6].

It is a well-known fact that all materials with a descending branch of the stress–strain relationship exhibit a strain localization which is not compatible to the continuum mechanics assumptions made in a finite element formulation. This makes the predictions to be mesh dependent (i.e. a finer mesh results in smaller ultimate limit loads) [7]. In order to alleviate this problem various localization limiters have been presented in the literature. Among the most well known limiters are (a) the crack band model [8] that uses a mesh-dependent softening modulus and may be expressed through the fracture energy that is considered to be a material parameter; (b) the non-local continuum model which assumes that the stress and strain are subjected to spatial averaging over a finite neighbourhood of a point [9], and (c) the gradient model which incorporates higher-order gradients into the constitutive law [10].

A simpler smeared crack model has been developed by Kotsovos and Pavlovic [11], based on experimental tests of concrete under multiaxial stress states [12], where cracking is treated as a complete sudden loss of stress [13]. This model, therefore, ignores any effect of material strain softening both in tension and compression. It is stated that a falling branch is a direct result of the control of crack propagation imposed by the machine in the course of testing [14, 15]. The only parameter needed for this model is the strength that can be obtained experimentally with a simple uniaxial cylinder compressive test. For mesh dependency in connection to finer meshes, it is argued that the experimental conditions under which the constitutive relations were derived limit the size of a finite element to be no less than two or three times the size of the maximum aggregate in the concrete mix and therefore no consideration of finer meshes is needed.

In the literature, almost all the static cyclic loading analyses of reinforced concrete structures, even for three-dimensional problems, use two-dimensional plane finite elements or fibre beam elements; for example, among the more recent ones are References [16–18]. There have appeared, however, some that have used three-dimensional solid elements, for example References [19, 20].

As far as dynamic analysis is concerned, the published work refers almost exclusively to plane problems. Agrawal and Jaeger [21] have used plane stress elements to compare the peak values response under seismic loading with existing test data for a shear wall specimen. NUPEC [22] has performed seismic ultimate dynamic response tests and its results for a shear wall specimen have been compared by Inoue *et al.* [23] who analysed it as a quasi-three-dimensional structure composed of plane elements. The same specimen has been analysed by Ile and Reynouard [24] using a crack band model together with two-dimensional plane elements. Mazars *et al.* [25] developed an equivalent two-dimensional reinforced

concrete model using lattice meshes for concrete and reinforcement bars and uniaxial constitutive laws based on continuum damage mechanics and plasticity. The analysis results of this model were also compared with NUPECs experimental data. A fracture energy-based rotating crack model was used by Han *et al.* [26] to analyse a shear wall and a plane frame structure with two-dimensional plane elements. Results were compared with shaking table experimental data. Kwan and Billington [27] analysed post-tensioned concrete bridge piers using plane elements. Only works of Faria *et al.* [28] and the very recent works of Mirzabozorg and Ghaemian [29] are known to the authors to have used a three-dimensional concrete element to analyse dams. Damage models having relatively few material parameters are proposed.

A critical issue in the non-linear analysis of RC structures is non-convergence and in case of convergence, it should be towards a realistic solution. In this work, the 3D solid finite element of Reference [11] that uses the uniaxial compressive strength as the only material parameter, as aforementioned, forms the basis to simulate the response of RC structures under dynamic loading. Preliminary results of this work were reported in Reference [30]. This model, in the case of monotonic loading, has given good predictions of failure loads. A crack strategy is proposed herein, which may handle in a most natural way the possible opening or closure of cracks. This procedure appears to have good convergence characteristics and its combination with the Newmark numerical integration method leads to a stable numerical process. This process is applied to the seismic analyses of two structures, for which experimental results exist, and shows good prediction of their dynamic response.

## 2. BRIEF REVIEW OF THE CONCRETE MODELLING

The concrete modelling used by Kotsovos and Pavlovic [11] will be briefly described in the following.

### 2.1. Constitutive modelling

The three-dimensional constitutive behaviour of concrete prior to macrocracking, when concrete suffers a noticeable loss of continuity, may be described with reference to the octahedral stress which may be decomposed into a hydrostatic $\sigma_0$ and a deviatoric part $\tau_0$. The following assumptions are made concerning their corresponding strains $\varepsilon_0$ and $\gamma_0$:

- Under pure hydrostatic stress, concrete only develops hydrostatic strains $\varepsilon_{0h}$.
- Deviatoric stress–strain relationships are almost independent of the applied hydrostatic stress.
- Under deviatoric stress, concrete also develops hydrostatic strains $\varepsilon_{0d}$, the values of which depend on the level of hydrostatic stress. This is the only significant form of coupling between the deviatoric stress and volume change.
- The behaviour is essentially isotropic.
- Unloading and subsequent reloading follow the initial stiffness slope (Figure 1).

In view of the above, the stress–strain relationship may be written in the following form:

$$\varepsilon_0 = \varepsilon_{0h} + \varepsilon_{0d} = \frac{\sigma_0 + \sigma_{id}}{3K_s}$$

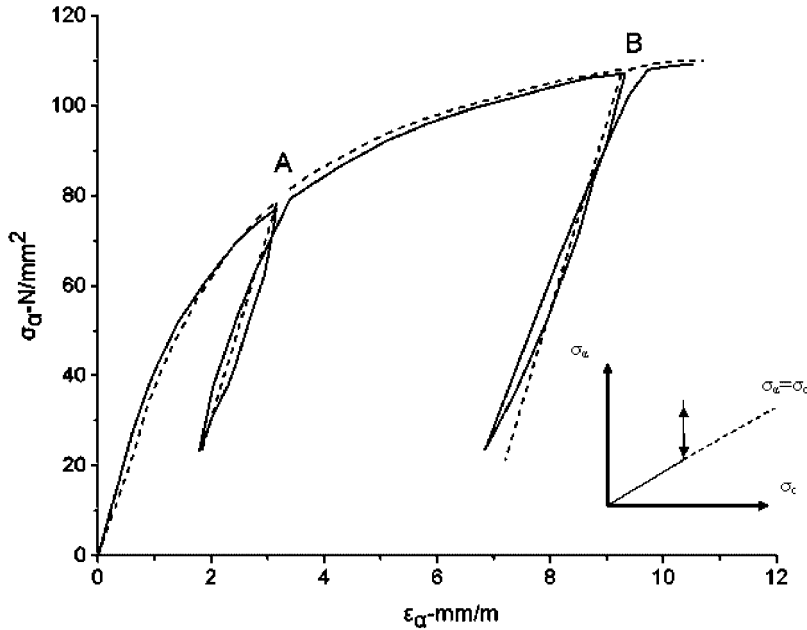$$\gamma_0 = \frac{\tau_0}{2G_s} \tag{1}$$

Figure 1. Measured and analytical stress–strain concrete behaviour during loading, unloading/reloading under triaxial compression.

where $\sigma_{id}(\sigma_0, \tau_0, f_c)$ is an equivalent internal hydrostatic stress that accounts for the coupling and $f_c$ is the uniaxial compressive strength of concrete; $K_s(\sigma_0, f_c)$ and $G_s(\tau_0, f_c)$ are secant bulk and shear moduli, respectively, should such a coupling not exist (i.e. they are obtained ignoring $\sigma_{id}$). Expressions for $\sigma_{id}, K_s$, and $G_s$ may be derived through curve fitting of experimental uniaxial, biaxial and triaxial data.

Since $\sigma_{id}$ is a pure hydrostatic correction, expressions (1) are equivalent to the following relations in global co-ordinate directions:

$$\varepsilon_{ij} = \frac{\sigma_{ij} + \sigma_{id}\delta_{ij}}{2G_s} - \frac{3v_s}{E_s}(\sigma_0 + \sigma_{id})\delta_{ij} \tag{2}$$

where $E_s(\sigma_0, \tau_0, f_c)$ and $v_s(\sigma_0, \tau_0, f_c)$ are secant Young's modulus and Poisson's ratio derived from $K_s$ and $G_s$, using standard formulae of linear elasticity:

$$\begin{aligned} E_s &= \frac{9K_s G_s}{3K_s + G_s} \\ v_s &= \frac{3K_s - 2G_s}{6K_s + 2G_s} \end{aligned} \tag{3}$$

Since the component of the non-linear deformation of concrete under $\tau_0$ is considerably larger than under $\sigma_0$ [31], if we denote by $\max \tau_0$ the deviatoric stress at each point on the stress–strain curve, then elastic unloading/reloading occurs whenever during a loading program the deviatoric stresses $\tau_0$ become less than $\max \tau_0$ (Figure 1, e.g. points A or B).
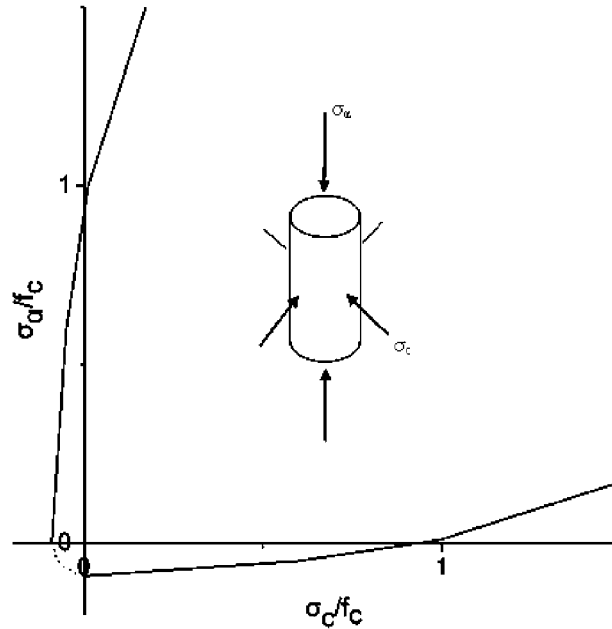
Figure 2. Intersection of failure surface for concrete with plane formed by space diagonal
and one of the principal axes.

The octahedral stresses also serve as a means to describe concrete failure which may be
represented in the three-dimensional principal stress space by an open and convex failure
surface. The form of such a failure surface can be seen in Figure 2, indicating the very small
strength of concrete under tensile stresses (positive axes refer to compressive stresses).

The projection of the failure surface on the deviatoric plane which is normal to $\sigma_0$ results
in a curve which is the locus of the ultimate deviatoric stress $\tau_{0u}$. This ultimate stress may
be calculated from $\sigma_0$ and $\theta$, where $\theta$ is the rotational angle that the deviatoric stress, taken
as a vector, forms with one of the projected stress principal axes on the deviatoric plane.

For a given state of stress the quantities $\sigma_0, \tau_0, \theta$ may be calculated:

$$\sigma_0 = \tfrac{1}{3}I_1$$

$$\tau_0 = \sqrt{\left(2\sigma_0^2 - \tfrac{2}{3}I_2\right)} \tag{4}$$

$$\cos 3\theta = -\frac{\sqrt{2}}{\tau_0^3}J_3$$

where $I_1$ and $I_2$ are the first and second invariants of the stress tensor, whereas $J_3$ is the third
invariant of the deviatoric stress tensor $s_{ij} = \sigma_{ij} - \sigma_0\delta_{ij}$.

It is an experimentally documented fact that when compressive stresses reach certain values,
concrete starts to increase its volume. Due to concrete in-homogeneity, such a localized re-
gion under compression then tends to expand against the surrounding material. The confining

concrete therefore introduces in the localized region lateral compressive stresses, which, in turn, for equilibrium to be maintained, make the surrounding regions develop tensile stresses. This has an effect of increasing the strength of the localized region while the tensile stresses in the surrounding region eventually turn this state of stress into having one of its principal components tensile. This, as can be seen from Figure 2, leads to the reduction of the strength of the surrounding region and macrocracking takes place.

### 2.2. Numerical modelling of cracking

A smeared fixed crack model within the framework of the finite element method is used to simulate the effect of cracking on the structure as the load is applied in small increments. Then, the increments of stresses at a Gauss point are found from the increments of strains through the adopted **D**-matrix (bold letters denote vectors and matrices):

$$\Delta\boldsymbol{\sigma} = \mathbf{D}\Delta\boldsymbol{\varepsilon} \tag{5}$$

So for an uncracked Gauss point

$$
\begin{bmatrix}
\Delta\sigma_x \\
\Delta\sigma_y \\
\Delta\sigma_z \\
\Delta\tau_{xy} \\
\Delta\tau_{xz} \\
\Delta\tau_{yz}
\end{bmatrix}
=
\begin{bmatrix}
2G+\mu & \mu & \mu & 0 & 0 & 0 \\
\mu & 2G+\mu & \mu & 0 & 0 & 0 \\
\mu & \mu & 2G+\mu & 0 & 0 & 0 \\
0 & 0 & 0 & G & 0 & 0 \\
0 & 0 & 0 & 0 & G & 0 \\
0 & 0 & 0 & 0 & 0 & G
\end{bmatrix}
\begin{bmatrix}
\Delta\varepsilon_x \\
\Delta\varepsilon_y \\
\Delta\varepsilon_z \\
\Delta\gamma_{xy} \\
\Delta\gamma_{xz} \\
\Delta\gamma_{yz}
\end{bmatrix}
\tag{6}
$$

where $\mu = vE/((1+v)(1-2v))$.

Since the relations are in incremental form, the above material constants are tangent ones. They may be evaluated [11] by differentiation from the secant material constants and are functions of $\sigma_0, \tau_0$.

When the failure surface at a Gauss point has been exceeded for the first time a crack perpendicular to the maximum tensile stress is formed. Suppose that the plane of the crack is OAB (Figure 3). Then for the local axis $z'$, which is perpendicular to this plane, the corresponding stiffnesses are zeroed, whereas a small shear is allowed to be transmitted in this plane denoted by $\beta G$. The shear retention factor $\beta$ is set equal to 0.1, mainly for convergence, simulating, however, in a way, some 'aggregate interlock' that has also been verified experimentally. The incremental stress–strain relationship then looks like the following:

$$
\begin{bmatrix}
\Delta\sigma'_x \\
\Delta\sigma'_y \\
\Delta\sigma'_z \\
\Delta\tau'_{xy} \\
\Delta\tau'_{xz} \\
\Delta\tau'_{yz}
\end{bmatrix}
=
\begin{bmatrix}
2G+\mu & \mu & 0 & 0 & 0 & 0 \\
\mu & 2G+\mu & 0 & 0 & 0 & 0 \\
0 & 0 & 0 & 0 & 0 & 0 \\
0 & 0 & 0 & G & 0 & 0 \\
0 & 0 & 0 & 0 & \beta G & 0 \\
0 & 0 & 0 & 0 & 0 & \beta G
\end{bmatrix}
\begin{bmatrix}
\Delta\varepsilon'_x \\
\Delta\varepsilon'_y \\
\Delta\varepsilon'_z \\
\Delta\gamma'_{xy} \\
\Delta\gamma'_{xz} \\
\Delta\gamma'_{yz}
\end{bmatrix}
\tag{7a}
$$

If a tensile state of stress is reached for the second time, then the plane that is perpendicular to the direction of the new maximum principal tensile stress together with the previous plane
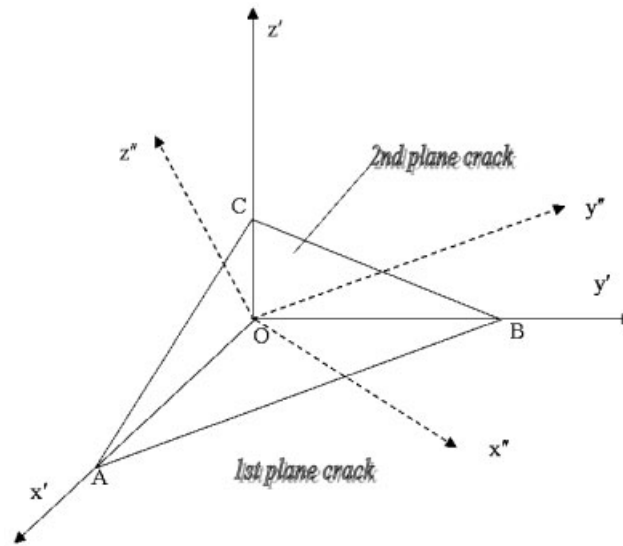
Figure 3. Local axes for one and two cracks at a Gauss point.

leaves only stiffness along the intersection of the two (Figure 3 line AB or the direction $y''$).
Thus, the incremental stress in terms of the incremental strains along these Cartesian axes
$(x''y''z'')$ is given by

$$
\begin{bmatrix} \Delta\sigma_x'' \\ \Delta\sigma_y'' \\ \Delta\sigma_z'' \\ \Delta\tau_{xy}'' \\ \Delta\tau_{xz}'' \\ \Delta\tau_{yz}'' \end{bmatrix} = \begin{bmatrix} 0 & 0 & 0 & 0 & 0 & 0 \\ 0 & 2G+\mu & 0 & 0 & 0 & 0 \\ 0 & 0 & 0 & 0 & 0 & 0 \\ 0 & 0 & 0 & \beta G & 0 & 0 \\ 0 & 0 & 0 & 0 & \beta G & 0 \\ 0 & 0 & 0 & 0 & 0 & \beta G \end{bmatrix} \begin{bmatrix} \Delta\varepsilon_x'' \\ \Delta\varepsilon_y'' \\ \Delta\varepsilon_z'' \\ \Delta\gamma_{xy}'' \\ \Delta\gamma_{xz}'' \\ \Delta\gamma_{yz}'' \end{bmatrix} \quad (7b)
$$

Because of the crack induced anisotropy for the last two cases, the stress–strain matrix,
expressed in local axes, is transformed to global orientations using the standard co-ordinate
system transformation laws.

If a new tensile stress occurs at the same Gauss point for a third time, then we have a
complete loss of carrying capacity of the Gauss point.

## 3. PROPOSED NUMERICAL STRATEGY

A single crack approach (SCA) has been used by Kotsovos and Spiliopoulos [32] in analyses
of reinforced concrete structures with crack closure. According to this strategy, the load is
applied in relatively large steps and for convergence reasons only one crack is allowed to open
or close inside a Newton–Raphson iteration. The check for the state of loading or unloading

at a Gauss point is determined at the beginning of the load step and remains fixed until convergence. Also, operations concerning closing or opening of cracks are done separately inside the load step. The first part of the load step deals exclusively with the closure of the cracks that are due to closing, whereas the second part of the load step caters only for the possible opening of new ones.

In the present paper, a new numerical strategy for the crack opening and closure is proposed. According to this strategy, which in the sequel will be called unified total crack approach (UTCA), the crack history of an integration point is treated in a unified way without separating the crack opening/closure in an iterative Newton–Raphson procedure. The check for loading or unloading at a Gauss point is done inside an iteration. Thus, the possibility of a Gauss point being in two different loading states inside a loading step is also included. The whole procedure, therefore, presents a more natural way of treating the non-linear process and therefore alleviates problems encountered with SCA [30].

According to the proposed procedure, if we denote by $j$ an iteration inside an incremental load step we can get an increment of displacements, using the tangent stiffness matrix of the previous iteration. Focusing on a Gauss point

1. The increments of strains are evaluated from the increments of the displacements

$$\Delta\boldsymbol{\varepsilon}^{(j)} = \mathbf{B}_\mathrm{c}\Delta\mathbf{u}^{(j)} \tag{8}$$

   where $\mathbf{B}_\mathrm{c}$ is the compatibility matrix of the concrete element.
2. The total strains are calculated from the strains of the previous iteration

$$\boldsymbol{\varepsilon}^{(j)} = \boldsymbol{\varepsilon}^{(j-1)} + \Delta\boldsymbol{\varepsilon}^{(j)} \tag{9}$$

3. A prediction of stresses is made using the material matrix of the previous iteration

$$\boldsymbol{\sigma}_\mathrm{pr}^{(j)} = \boldsymbol{\sigma}^{(j-1)} + \mathbf{D}^{(j-1)}\Delta\boldsymbol{\varepsilon}^{(j)} \tag{10}$$

From the predicted state of stress the quantities $\tau_0^{(j)}, \sigma_0^{(j)}$ and $\tau_{0\mathrm{u}}^{(j)}$ may be calculated. A correction of stress occurs depending on whether the Gauss point was at the previous iteration cracked or uncracked.

For an *uncracked* Gauss point, all the different possibilities may be traced in Figure 4.

If $\tau_0^{(j)}$ is found larger than $\tau_{0\mathrm{u}}^{(j)}$, something which normally happens when tensile stresses have developed, a new crack forms normal to the direction of the maximum principal tensile stress $\sigma_I$. This stress is put to zero without the other two principal stresses being affected. This has an effect to produce residual stresses:

$$\Delta\boldsymbol{\sigma}_\mathrm{r} = \mathbf{T}_\sigma^{-1} \cdot \left\{\begin{array}{c} -\sigma_I \\ 0 \\ 0 \end{array}\right\} \tag{11}$$

where $\mathbf{T}_\sigma^{-1}$ is the inverse transformation matrix from the principal stress axes to the initial $x, y, z$ axes.

At the same time the material matrix in terms of the local crack's axis is established using Equation (7a). The transformation of this matrix to the global axes, denoted by $\mathbf{D}_\mathrm{cr}^{(j)}$, updates the material matrix $\mathbf{D}^{(j)}$ to be used in the next iteration.
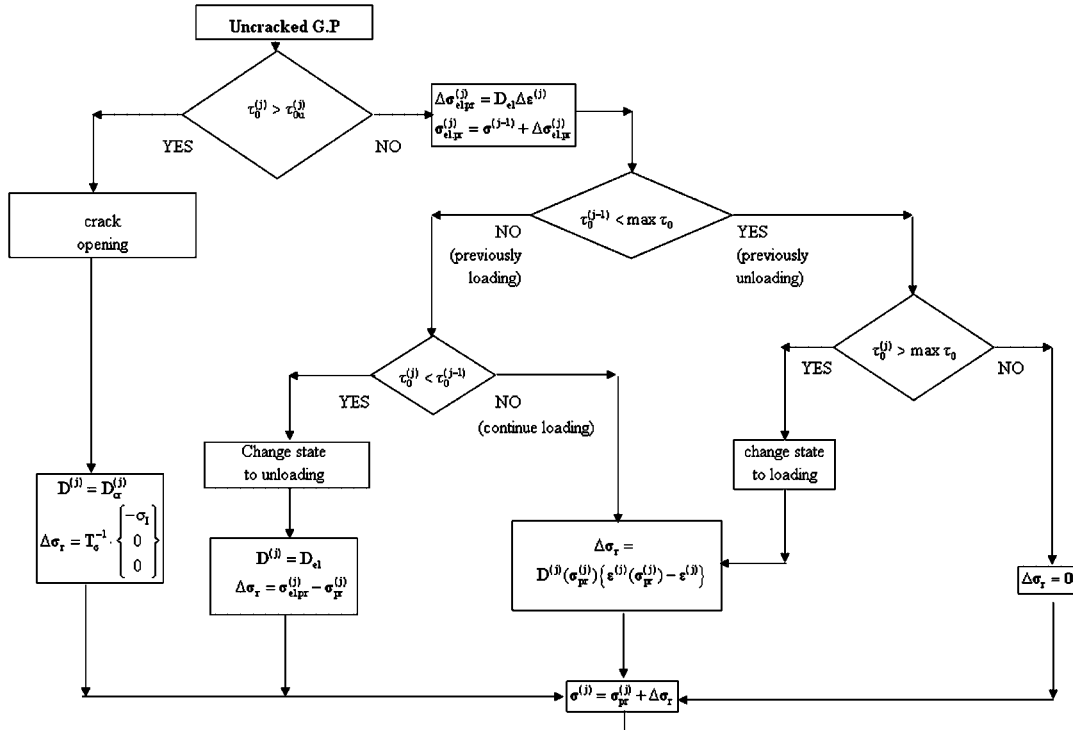
Figure 4. Flow chart for the stress correction at an uncracked Gauss point.

For a Gauss point that remains uncracked an elastic stress prediction is performed:

$$\Delta\boldsymbol{\sigma}_{\mathrm{el.pr}}^{(j)} = \mathbf{D}_{\mathrm{el}}\Delta\boldsymbol{\varepsilon}^{(j)}$$

$$\boldsymbol{\sigma}_{\mathrm{el.pr}}^{(j)} = \boldsymbol{\sigma}^{(j-1)} + \Delta\boldsymbol{\sigma}_{\mathrm{el.pr}}^{(j)} \tag{12}$$

where $\mathbf{D}_{\mathrm{el}}$ is the material matrix that contains the initial material constants.

Next it has to be determined whether the Gauss point is in a condition of previously loading $(\tau_0^{(j-1)} > \max \tau_0)$ or unloading $(\tau_0^{(j-1)} < \max \tau_0)$.

For a previously loading Gauss point that is further loaded $(\tau_0^{(j)} > \tau_0^{(j-1)})$ or a previously unloading Gauss point that changes its state to loading $(\tau_0^{(j)} > \max \tau_0)$, an initial strain method [11] is applied and the stress is corrected according to

$$\Delta\boldsymbol{\sigma}_{\mathrm{r}} = \mathbf{D}^{(j)}(\boldsymbol{\sigma}_{\mathrm{pr}}^{(j)})\{\boldsymbol{\varepsilon}^{(j)}(\boldsymbol{\sigma}_{\mathrm{pr}}^{(j)}) - \boldsymbol{\varepsilon}^{(j)}\} \tag{13}$$

where $\boldsymbol{\varepsilon}^{(j)}(\boldsymbol{\sigma}_{\mathrm{pr}}^{(j)})$ is computed according to Equation (2). If a previously unloading Gauss point continues to unload $(\tau_0^{(j)} < \max \tau_0)$, then no stress correction is needed $(\Delta\boldsymbol{\sigma}_{\mathrm{r}} = \mathbf{0})$.

In the last case where a previously loading uncracked Gauss point begins to unload $(\tau_0^{(j)} < \tau_0^{(j-1)})$, initial elastic properties are restored and the residual stresses are equal to the difference
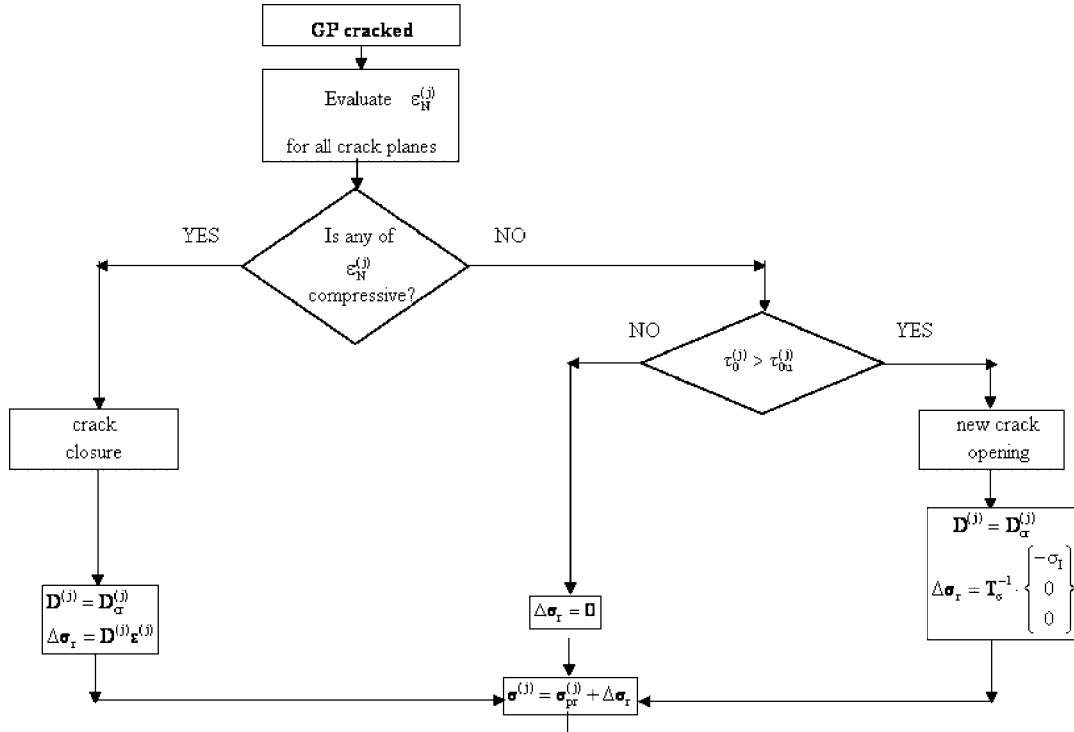
Figure 5. Flow chart for the stress correction at a cracked Gauss point.

of the elastically predicted stresses and the tangent predicted stresses:

$$\Delta\boldsymbol{\sigma}_{\mathrm{r}} = \boldsymbol{\sigma}_{\mathrm{el.pr}}^{(j)} - \boldsymbol{\sigma}_{\mathrm{pr}}^{(j)} \tag{14}$$

For a *cracked* Gauss point the different possibilities may be found in Figure 5.

The total strains normal to all the existing crack directions $\varepsilon_{\mathrm{N}}^{(j)}$ are checked and if any one of them is found compressive, the crack is assumed to close, the material matrix in the local crack's direction is updated using Equations (7a) and (7b) and the transformed to the global stress directions $\mathbf{D}_{\mathrm{cr}}^{(j)}$ is set equal to $\mathbf{D}^{(j)}$. At the same time the stresses are corrected using this matrix and the total strains:

$$\Delta\boldsymbol{\sigma}_{\mathrm{r}} = \mathbf{D}^{(j)}\boldsymbol{\varepsilon}^{(j)} \tag{15}$$

In case there is no crack closure the procedure checks whether we have a crack opening ($\tau_0^{(j)} > \tau_{0\mathrm{u}}^{(j)}$). If this happens, then the stress correction may be done using Equation (11); otherwise no stress correction is needed ($\Delta\boldsymbol{\sigma}_{\mathrm{r}} = \mathbf{0}$).

For both the cases of the cracked or uncracked Gauss points the stress corrections give rise to unbalanced forces that are implemented, in the standard way, as a new force vector applied in the next iteration.
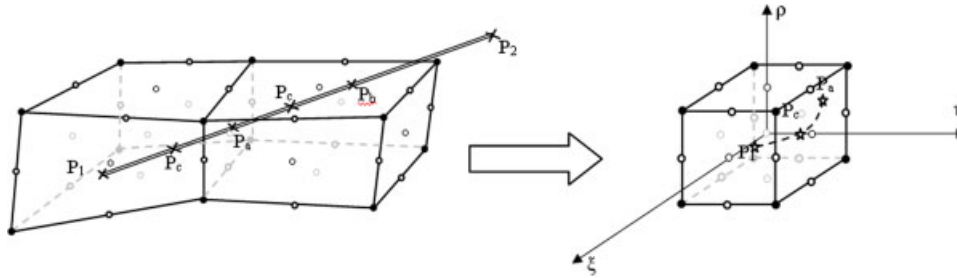
Figure 6. Embedding a straight steel bar inside concrete.

Twenty seven-node Lagrangian brick elements with $3 \times 3 \times 3$ Gauss points were used for the finite element implementation of concrete behaviour. The well-known fact of mesh in-objectivity for brittle materials [7] (although not so pronounced when reinforcement exists) is circumvented using elements having a size of 5–20 cm that have proved to give realistic results. This is due to the fact that the size of the concrete specimens that were used to deduce the above-described concrete behaviour is roughly the same as the equivalent volume that corresponds to a Gauss point. This size of elements therefore serves as a means of a 'localization limiter'.

Steel bars are modelled as three-noded uniaxial truss elements. The Menegotto–Pinto [33] model is adopted; this model accommodates the Bauschinger effect, observed in steel, under large load reversals. Inside an iteration of an incremental step, in the standard way, the incremental strain along the steel bars is used to make an elastic prediction for the stress. If this stress is found to be larger than the current yield stress, a correction to the stress is made so that it is brought back on the true stress–strain curve. Equivalent nodal stresses are then applied so that equilibrium is restored.

Steel bars may be considered to have arbitrary positions inside the concrete elements (Figure 6). A numerical procedure that takes into account the contribution of such an embedded reinforcement is used. With this procedure for each straight segment of reinforcement only the end point co-ordinates in the global axes need to be provided by the analyst. The concrete elements that contain a portion of the bar defined through the points $P_1$ and $P_2$ may be found with the aid of a reverse mapping from the global co-ordinates $(x, y, z)$ to the element natural ones $\xi, \eta, \rho$. A Newton–Raphson procedure is utilized to make this conversion [34]. The point $P_1$ is contained in a given concrete element if its co-ordinates $\xi_{P_1}, \eta_{P_1}, \rho_{P_1}$ satisfy

$$|\xi_{P_1}, \eta_{P_1}, \rho_{P_1}| \leqslant 1 \tag{16}$$

Once the element that contains $P_1$ is found, the use of analytic geometry determines the intersection point $P_a$ of $P_1 P_2$ with one of the possible six faces of the elements [35]. After this has been established, $P_1$ becomes $P_a$ and the algorithm is repeated.

Assuming a perfect bond between steel and concrete, the strain inside iteration $j$ of the incremental step along the steel bar with direction cosines $l, m, n$ may easily be evaluated [36]:

$$\Delta \varepsilon_{\mathrm{r},xx}^{(j)} = \Delta \varepsilon_{xx}^{(j)} l^2 + \Delta \varepsilon_{yy}^{(j)} m^2 + \Delta \varepsilon_{zz}^{(j)} n^2 + 2 \Delta \varepsilon_{xy}^{(j)} lm + 2 \Delta \varepsilon_{yz}^{(j)} mn + 2 \Delta \varepsilon_{xz}^{(j)} ln$$

$$= \mathbf{T}_\varepsilon \Delta \boldsymbol{\varepsilon}^{(j)} = \mathbf{T}_\varepsilon \mathbf{B}_\mathrm{c} \Delta \mathbf{u}^{(j)} = \mathbf{B}_\mathrm{r} \Delta \mathbf{u}^{(j)} \tag{17}$$

The contribution to the stiffness matrix of a steel bar inside a concrete element is given by

$$\mathbf{K}_r^{(j)} = A_r E^{(j)} \int_S \mathbf{B}_r^T \mathbf{B}_r \, dS \tag{18}$$

where $E_r^{(j)}$ and $A_r$ are the tangential modulus of elasticity and the cross-sectional area of the steel bar. Thus, the total stiffness matrix of the reinforced concrete element is

$$\mathbf{K}^{(j)} = \mathbf{K}_c^{(j)} + \sum_{i=1}^{nrs} \mathbf{K}_{r,i}^{(j)} = \int_V \mathbf{B}_c^T \mathbf{D}^{(j)} \mathbf{B}_c \, dV + \sum_{i=1}^{nrs} \mathbf{K}_{r,i}^{(j)} \tag{19}$$

where *nrs* is the number of embedded reinforcements inside a brick element.

A highly modular finite element code (FE77 [37]) was used as a basis for the implementation of the above-described procedures. A new module was added in which the Newton–Raphson iterative procedure with the mathematical description of concrete behaviour, together with the different approaches regarding the crack strategy were implemented.

## 4. RC SHEAR WALL UNDER STATIC CYCLIC LOADING

The whole procedure was applied under a static displacement control to a reinforced concrete shear wall that was considered clamped at its base. The finite element model of the wall can be seen in Figure 7(a). The wall was 650 mm wide, 1300 mm high and 65 mm thick. Steel bars of 8 and 6.25 mm diameter with yield strength of 470 and 520 MPa were used as vertical and horizontal reinforcement, respectively. Additional reinforcement with the form of stirrups (4 mm diameter bars, 420 MPa yield strength) confined the wall edges. Concrete uniaxial compressive strength was 35.2 MPa. The wall was subjected to a series of four displacement saw-toothed loading cycles between the values of ±5 cm before a continuous increasing displacement was applied. Results (Figure 7(b)) were compared against existing experiments [38].

It can be seen that there is good ultimate load prediction together with good prediction at the ends of the cycles. The ultimate loading analytical prediction that is given by the last point for which the solution has converged (96 kN) is quite close to the maximum load given by the experiment (115 kN). Beyond this point the analysis diverges due to the extensive cracking in the compressive region of the wall.

It is obvious that the prediction of the energy dissipation is relatively poor. If a softening behaviour with secant unloading was modelled, the resulting dissipated energy could be larger. It is anticipated, nevertheless, that the dominant mechanism that creates energy dissipation in cyclic loading is related to the reinforcement. Since the nonlinearities of the steel bars are modelled accurately, it is expected that the possibility of including a bond-slip effect could enhance the model's behaviour towards a better dissipated energy prediction.

## 5. DYNAMIC ANALYSIS

Dynamic equilibrium at any instant of time *t* may be expressed in the form of the following equations:

$$\mathbf{M}\ddot{\mathbf{u}} + \mathbf{C}\dot{\mathbf{u}} + \mathbf{f}(\mathbf{u}) = \mathbf{p}(t) \tag{20}$$
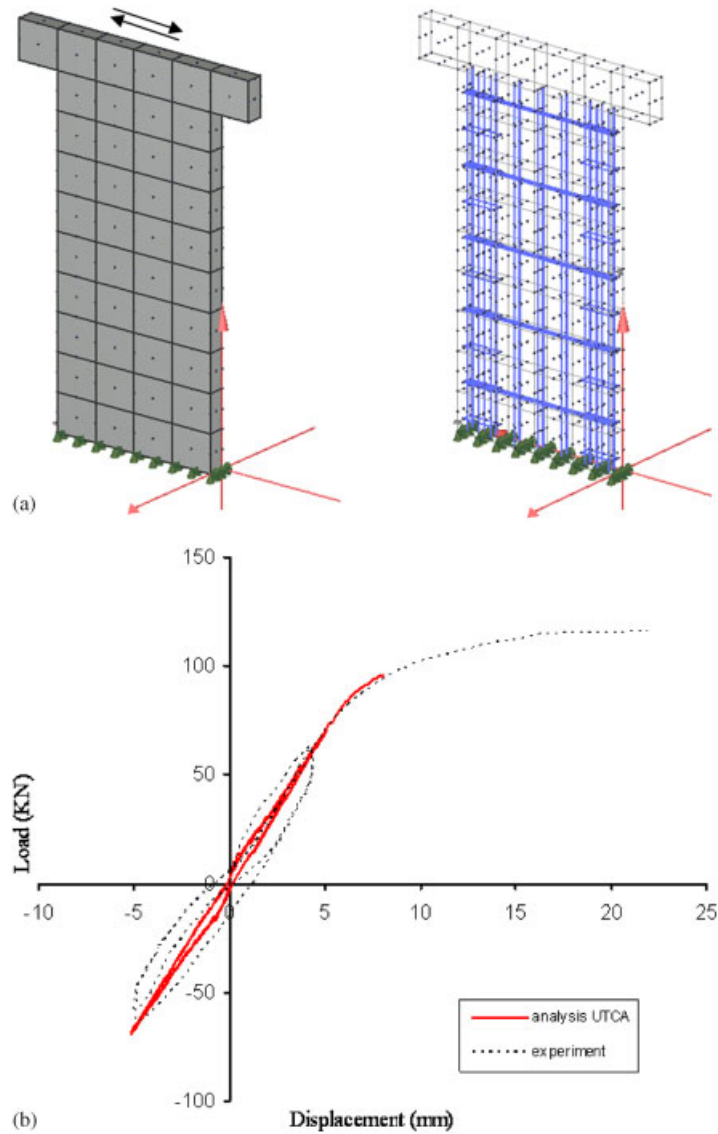
Figure 7. (a) Finite element modelling of reinforced concrete shear wall; and (b) comparison of analytical against experimental results under static cyclic displacement on a reinforced shear wall.

with **M** being the mass matrix, **C** a Rayleigh damping matrix, and **f(u)** the vector of internal forces. The applied loads $\mathbf{p}(t)$ are given by

$$\mathbf{p}(t) = -\mathbf{m}\ddot{u}_g(t) + \mathbf{p}_g \qquad (21)$$

where $\mathbf{p}_g$ is the external force vector due to the self weight of the structure, $\mathbf{m}$ a vector that contains the masses for all the degrees along the direction of the ground motion and $\ddot{u}_g(t)$ the ground acceleration.

The self-weight is applied in a static incremental step to find an initial displacement vector $\mathbf{u}_0$ as well as the initial internal force vector $\mathbf{f}_0$. A few iterations are needed for convergence.

Using the Newmark method, the problem may be converted to a series of static incremental steps [39]. The incremental load vector is formed according to Equations (22):

$$\Delta\mathbf{p}_i = -\mathbf{m}\Delta\ddot{u}_{g,i} = -\mathbf{m}(\ddot{u}_{g,i+1} - \ddot{u}_{g,i})$$

$$\Delta\hat{\mathbf{p}}_i = \Delta\mathbf{p}_i + \left(\frac{1}{\beta\Delta t}\mathbf{M} + \frac{\gamma}{\beta}\mathbf{C}\right)\dot{\mathbf{u}}_i + \left(\frac{1}{2\beta}\mathbf{M} + \Delta t\left(\frac{\gamma}{2\beta} - 1\right)\mathbf{C}\right)\ddot{\mathbf{u}}_i \tag{22}$$

where $i$ is the incremental step ($i = 0, 1, 2, \ldots$) and $\gamma, \beta$ the constants of Newmark's method.

Inside an incremental step an iterative procedure is performed, which calculates the augmented stiffness matrix at each iteration $j$:

$$\hat{\mathbf{K}}_{i+1}^{(j-1)} = \mathbf{K}_{i+1}^{(j-1)} + \frac{\gamma}{\beta\Delta t}\mathbf{C} + \frac{1}{\beta(\Delta t)^2}\mathbf{M} \tag{23}$$

where depending on the current state of the concrete Gauss point the tangent stiffness $\mathbf{K}_{i+1}^{(j-1)}$ may be calculated from Equation (19).

An increment of displacements $\Delta\mathbf{u}^{(j)}$ can be obtained from Equation (24):

$$\hat{\mathbf{K}}_{i+1}^{(j-1)}\Delta\mathbf{u}^{(j)} = \Delta\mathbf{R}^{(j-1)} \tag{24}$$

$\Delta\mathbf{R}$ is the increment of the residual forces, which, at the beginning of the first iteration, is equal to the incremental external force vector $\Delta\hat{\mathbf{p}}_i$, whereas for all subsequent iterations, it is calculated using the internal forces vector $\mathbf{f}$.

The increment of the displacements $\Delta\mathbf{u}^{(j)}$ can be used to update the total displacements:

$$\mathbf{u}_{i+1}^{(j)} = \mathbf{u}_{i+1}^{(j-1)} + \Delta\mathbf{u}^{(j)} \tag{25}$$

At the same time, from the increments of the displacements we may get a stress correction $\Delta\boldsymbol{\sigma}_r$ and an iterative stress $\boldsymbol{\sigma}^{(j)}$ according to the two flow charts of Figures 4 and 5 for the concrete elements. Analogous stress correction and iterative stresses may be derived for steel elements. Having these stresses we may get an update of the internal forces:

$$\mathbf{f}^{(j)} = \int_V \mathbf{B}^T\boldsymbol{\sigma}^{(j)} \, \mathrm{d}V \tag{26}$$

with $\mathbf{B}$ being either $\mathbf{B}_c$ or $\mathbf{B}_r$ for concrete or steel elements, respectively.

A convergence check is made whether

$$\frac{\|\Delta\mathbf{R}^{(j)}\|}{\|\Delta\hat{\mathbf{p}}_i\|} < \text{tol} \tag{27}$$

If Equation (27) is satisfied, then we update displacements, velocities and accelerations and proceed to the next incremental step; otherwise iterations continue till convergence.

Choosing a small time step assures stability and accuracy of the solution.

## 6. TWO-STOREY RC FRAMES UNDER SEISMIC LOAD

The numerical procedure presented above was tested against existing experimental results on two-storey reinforced concrete specimens under seismic loading. Two of these frames (named as L30 and H30) of identical dimensions but of different reinforcement detailing had been designed according to EC2 and EC8 and tested on the shake table of the Laboratory of Earthquake Engineering at the National Technical University of Athens. A detailed description of these tests can be found in a report published in 1997 [40].

According to the experimental data the two ground columns (C1) of these frames have cross-sectional dimensions of $200 \times 150$ mm and a clear length of 2860 mm, whereas the two first floor columns (C2) have a length of 1560 mm and the same cross-sectional dimensions as C1. The two beams B1 and B2 of the ground and the first floor, respectively, have a clear span of 2200 mm and overhangs of 300 mm with cross-sectional dimensions of $160 \times 150$ mm. The thickness of the two slabs was equal to 80 mm. Details of the reinforcement may be seen in Table I. The uniaxial concrete compressive strength was estimated to be 50 MPa whereas the steel bars showed a yield limit approximately equal to 500 MPa. Frame L30 was designed to exhibit moderately low ductility using a behavioural factor of $q = 2.5$, whereas the frame H30 was designed for higher ductility of $q = 5.0$.

The frames were tested under three ground motions of sinusoidal form applied in sequence. The three accelerograms exhibit a maximum approximate magnitude of one and two times the magnitude of the design ground acceleration of the frame which was $0.30g$. Additional masses were applied on the two slabs to simulate the live loads. The total weight of each specimen was approximately 120 kN.

A numerical modelling of these structures can be seen in Figure 8(a). Each structure was discretized by 27-node brick elements. Nine such elements were used to discretize each of the bottom columns and eight for each of the top columns. Twelve elements were used for the discretization of the two beams and 36 for the discretization of each of the two slabs. Using the embedded formulation it was a relatively easy task to input the steel bars. The denser reinforcement of stirrups at the critical region of the beam–column joints of the frame of higher ductility H30 may be seen (Figure 8(b)) compared to the one of the lower ductility (Figure 8(c)). Because of no significant experimental evidence of cracking in the

Table I. Detailing of reinforcement of the two RC frames.

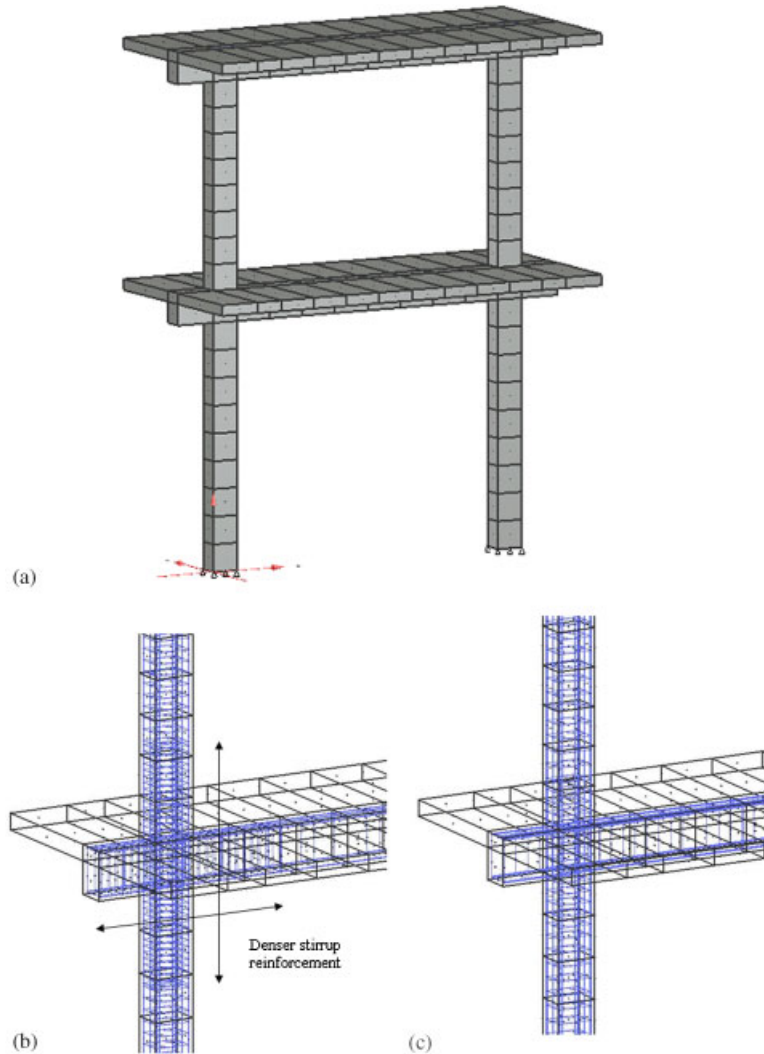| Specimen name | Member | Bottom steel | Top steel | Stirrups | |
| --- | --- | --- | --- | --- | --- |
| | | | | Critical region | Non-critical region |
| L30 | B1 | 2Φ12 | 2Φ12 | Φ4/130 | Φ4/130 |
| | B2 | 2Φ8 | 4Φ8 | Φ4/175 | Φ4/175 |
| | C1 | 12Φ8 | 8Φ8 | Φ4/55 | Φ4/75 |
| | C2 | 8Φ8 | 8Φ8 | Φ4/55 | Φ4/70 |
| H30 | B1 | 2Φ8 | 4Φ8 | Φ4/40 | Φ4/175 |
| | B2 | 2Φ8 | 2Φ8 | Φ4/40 | Φ4/175 |
| | C1 | 8Φ8 | 8Φ8 | Φ4/30 | Φ4/55 |
| | C2 | 8Φ8 | 8Φ8 | Φ4/30 | Φ4/55 |

Figure 8. (a) Layout and mesh of the RC frame; (b) detail of reinforcement at the joint of the frame of higher ductility; and (c) detail of reinforcement at the joint of the frame of lower ductility.

slabs, these were modelled as elastic. This reduces the amount of computational cost, since only a coarse discretization is needed and no material non-linearities are accounted for in that region. Additionally, the extra masses were taken into account by increasing the specific weight of concrete at the slab area by a factor of five (5).

An eigenvalue analysis using the initial elastic properties of the two structures showed time periods for the first two modes in the $x$ direction of $T_1 = 0.229$ s and $T_2 = 0.072$ s. These values, as expected, are lower than the experimental ones ($T_{1,\exp} = 0.303$ s and $T_{2,\exp} = 0.093$ s) mainly due to some minor cracking that exists, under static loading, in the real structure.
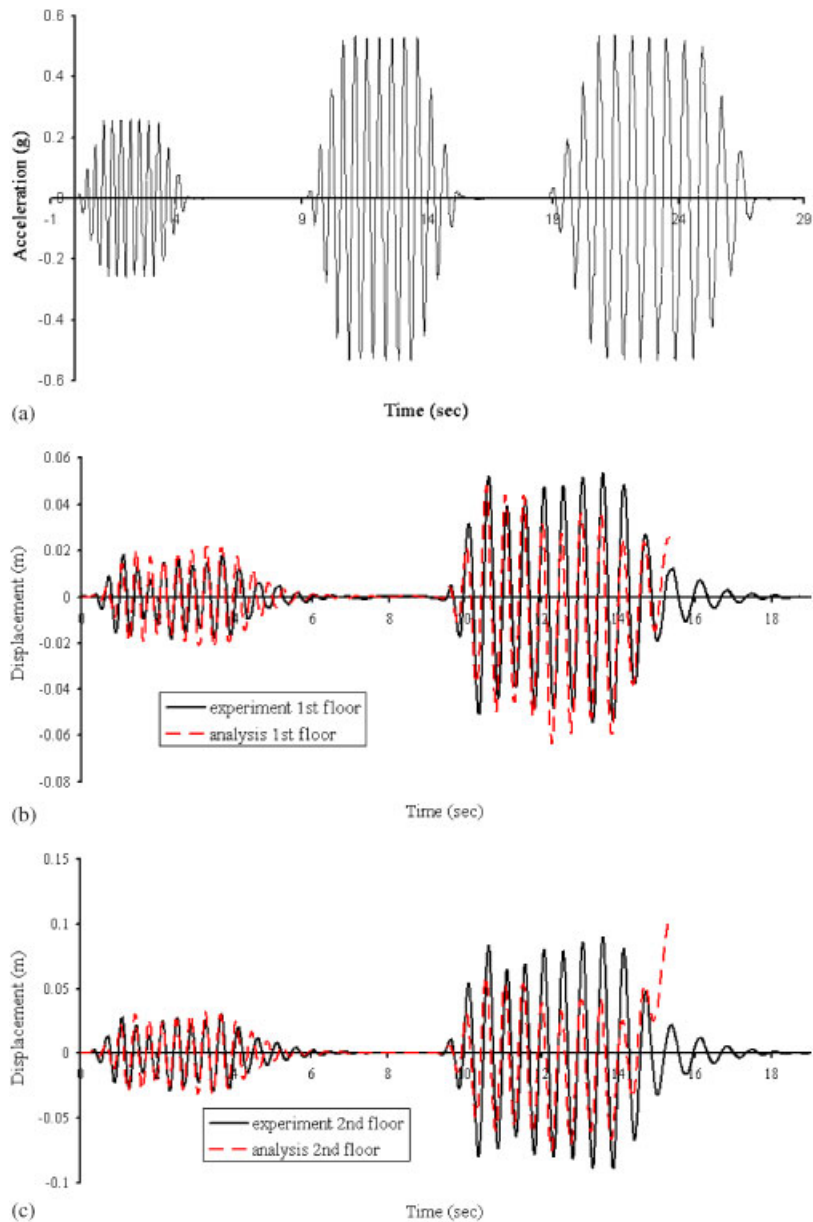
Figure 9. (a) Base acceleration of shake table for TEST1, TEST2 and TEST3 on specimen L30; (b) first floor response of specimen L30 under base motion TEST1 and TEST2; and (c) second floor response of specimen L30 under base motion TEST1 and TEST2.

A constant damping ratio of 3% for the first two modes was used. This value was chosen after some numerical experimentation with the two specimens to cater for all the energy dissipation mechanisms that are not included in the material model (for example, perfect
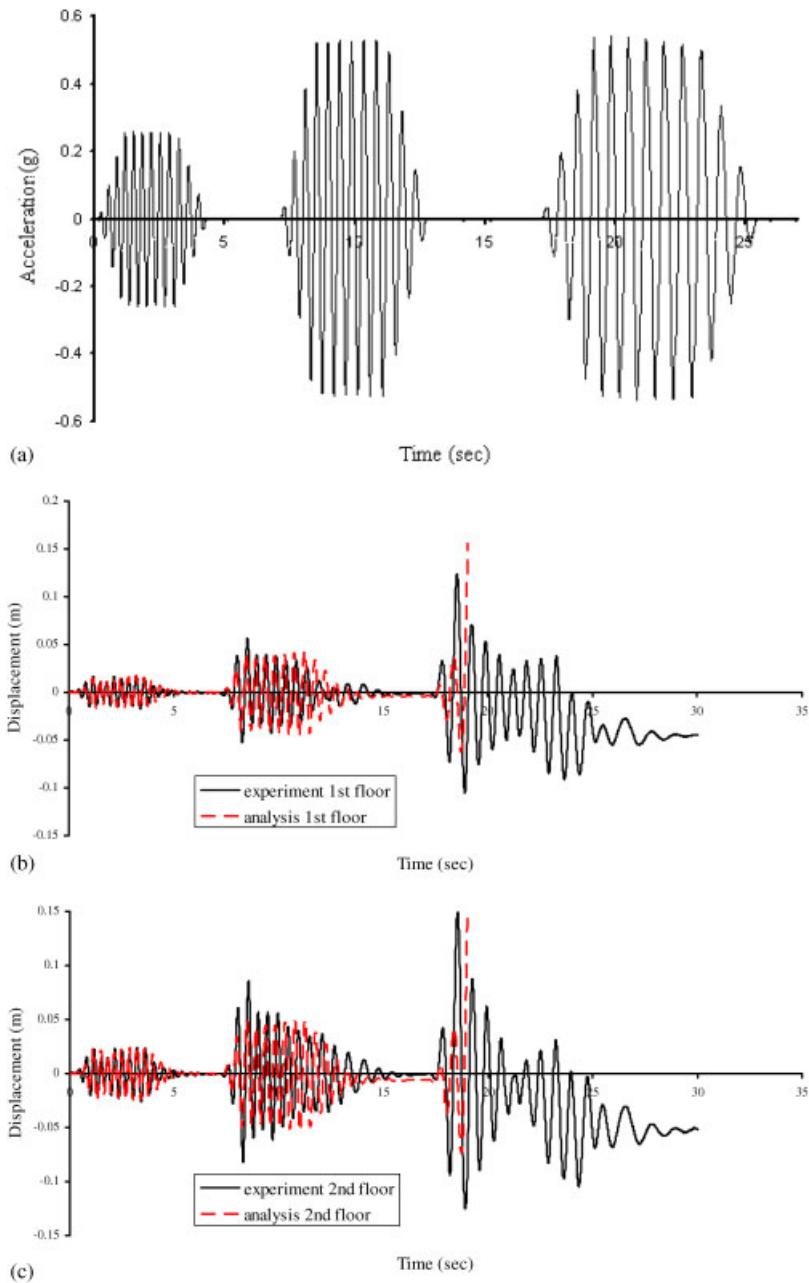
Figure 10. (a) Base acceleration of shake table for TEST1, TEST2 and TEST3 on specimen H30; (b) first floor response of specimen H30 under base motion TEST1, TEST2 and TEST3; and (c) second floor response of specimen H30 under base motion TEST1, TEST2 and TEST3.
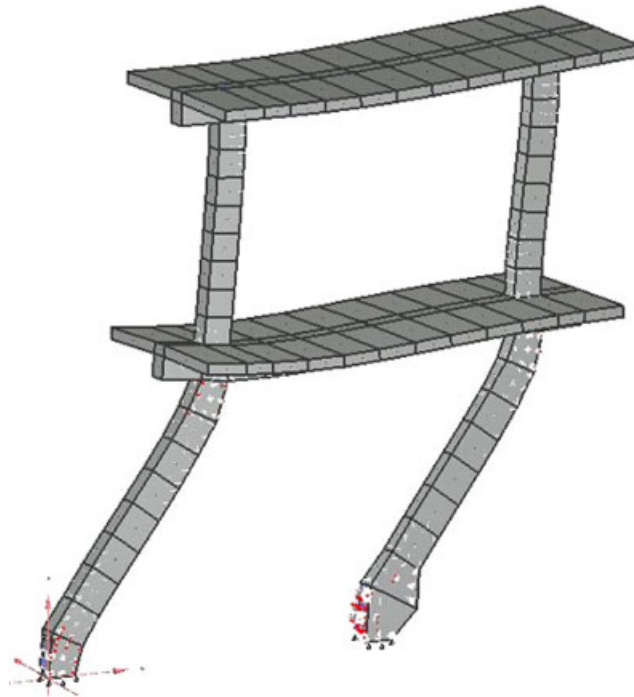
Figure 11. Collapse of RC frame H30 under the base acceleration of Figure 10(a). White marks indicate concrete cracking on the external surface.

bond between concrete and steel was assumed). The resulting factors for Rayleigh damping are 1.255 and $5.227 \times 10^{-4}$, respectively.

The two frames were subjected to the base acceleration shown in Figures 9(a) and 10(a), respectively (TEST1, TEST2 and TEST3). A time history analysis was performed using a time step of $\Delta t = 0.015$ s. The parameters for the Newmark numerical integration were $\beta = 0.25$ and $\gamma = 0.5$, so that the time integration is unconditionally stable.

Results (Figure 9(b) and (c)) for the frame L30, of lower ductility, show that the model predicts a realistic response for a dynamic loading approximately equal to the design load of the structure, which is a minimum requirement from an RC computational analysis. Moreover, although during TEST2 the structure exhibits considerable non-linear characteristics (extensive cracking and a large number of reinforcement bars yielding), stable solutions may still be obtained under a loading which is twice the magnitude of the design value. A deviation from the experimental results occurs towards the end of TEST2 and the solution diverges after its end.

The computed response is even closer to the experimental data for the case of specimen H30 (Figure 10(b) and (c)). The model simulates the response quite well for the first two accelerograms and only diverges in the second cycle of TEST3. It is obvious that the higher amount of reinforcement provides better stability and accuracy.

As far as cracking is concerned for both specimens, the predictions of the analyses compare well with the experimental crack patterns. The deformational mode of failure from the analysis of specimen H30 (Figure 11), which is similar to that of L30, shows extensive cracking and yielding of longitudinal and vertical reinforcement mainly at the top and bottom of the ground floor columns.

The main reason for the divergence of the calculations is believed to be the fact that the analysis reaches the limits of the proposed numerical concrete modelling. The smeared crack approach which assumes a continuous displacement field inside an element may not adequately describe the behaviour of the extensively damaged regions of the reinforced concrete frame at load levels as large as twice the order of magnitude of the design.

## 7. CONCLUSIONS

In this work, a relatively simple 3D solid concrete element is used to estimate the dynamic response of reinforced concrete structures. The simplicity of the model lies in the fact that the only concrete material parameter that needs to be supplied by the analyst is its uniaxial compressive strength. A loading–unloading strategy is proposed, which when combined with this concrete model renders a procedure that produces convergent results, something which is always difficult to achieve in the non-linear analysis of reinforced concrete structures. Good agreement of the numerical results with experimental data is observed.

### REFERENCES

 1. Rashid YR. Analysis of prestressed concrete pressure vessels. *Nuclear Engineering Design* 1968; **7**(4):334–344.
 2. Gupta AK, Akbar H. Cracking in reinforced concrete analysis. *Journal of Structural Engineering* 1984; **110**: 1735–1746.
 3. Crisfield MA, Wills J. Analysis of RC panels using different concrete models. *Journal of Engineering Mechanics* 1989; **115**(3):578–597.
 4. Bazant ZP, Caner FC, Carol I, Adley MD, Akers SA. Microplane model M4 for concrete I: formulation with work—conjugate deviatoric stress. *Journal of Engineering Mechanics* 2000; **126**:944–953.
 5. Caner FC, Bazant ZP. Microplane model M4 for concrete II: algorithm and calibration. *Journal of Engineering Mechanics* 2000; **126**:954–961.
 6. Jirasek M, Bazant ZP. *Inelastic Analysis of Structures*. Wiley: West Sussex, England, 2002.
 7. Bazant ZP. Instability ductility and size effect in strain softening concrete. *Journal of Engineering Mechanics* 1976; **102**:331–344.
 8. Bazant ZP, Oh B. Crack band theory for fracture of concrete. *RILEM Materials and Structures* 1983; **16**: 155–177.
 9. Bazant ZP. Imbricate continuum and its variational derivation. *Journal of Engineering Mechanics* 1984; **110**(12):1693–1712.
10. de Borst R, Muhhaus HS. Gradient-dependent plasticity: formulation and algorithmic aspects. *International Journal for Numerical Methods in Engineering* 1992; **35**:521–539.
11. Kotsovos MD, Pavlovic MN. Structural concrete. *Finite Element Analysis for Limit State Design*. Thomas Telford: London, 1995.
12. Kotsovos MD, Newman JB. Generalized stress–strain relations for concrete. *Journal of the Engineering Mechanics Division Proceedings* 1978; **104**:845–856.

13. Kotsovos MD. A mathematical description of the strength properties of concrete under generalized stress. *Magazine of Concrete Research* 1979; **31**(108):151–158.
14. van Mier JGM *et al*. Strain softening of concrete in uniaxial compression. *RILEM Materials and Structures* 1997; **30**:195–209.
15. Zisopoulos PM, Kotsovos MD, Pavlovic MN. Deformational behaviour of concrete specimens in uniaxial compression under different boundary conditions. *Cement and Concrete Research* 2000; **30**:153–159.
16. Kwan WP, Billington SL. Simulation of structural concrete under cyclic load. *Journal of Structural Engineering* 2001; **127**:1391–1401.
17. Kwan WP, Billington SL. Unbonded posttensioned concrete bridge piers. I: monotonic and cyclic analyses. *Journal of Bridge Engineering* 2003; **8**:92–101.
18. Mazars J, Ragueneau F, Casaux G, Colombo A, Kotronis P. Numerical modeling for earthquake engineering: the case of lightly RC structural walls. *International Journal for Numerical and Analytical Methods in Geomechanics* 2004; **28**:857–874.
19. Girard C, Bastien J. Finite element bond slip model for concrete columns under cyclic loads. *Journal of Structural Engineering* 2002; **128**:1502–1510.
20. Ozbolt J, Li YJ. Three dimensional cyclic analysis of compressive diagonal shear failure. In *Finite Element Analysis of RC Structures*, Willam K, Tanabe T (eds). ACI International, Farmington Hills, MI, 2001; ACI-SP-205-4:61–79.
21. Agrawal AB, Jaeger LG. Response of RC shear wall under ground motions. *Journal of the Structural Division Proceedings* 1981; **107**(2):395–411.
22. OECD Nuclear Energy Agency. Committee on the safety of nuclear installations, seismic shear wall ISP. *NUPEC's Seismic Ultimate Dynamic Response Test—Comparison Report*, 1996, NEA/CSNI/R(96)10.
23. Inoue N, Yang K, Shibata A. Dynamic nonlinear analysis of RC shear wall by fem with explicit analytical procedure. *Earthquake Engineering and Structural Dynamics* 1997; **26**:967–986.
24. Ile N, Reynouard JM. Nonlinear analysis of reinforced concrete shear wall under earthquake loading. *Journal of Earthquake Engineering* 2000; **4**(2):83–213.
25. Mazars J, Kotronis P, Davenne L. A new modelling strategy for the behaviour of shear walls under dynamic loading. *Earthquake Engineering and Structural Dynamics* 2002; **31**:937–954.
26. Han TS, Billington SL, Ingraffea AR. Simulation strategies to predict seismic response of RC structures. *Finite Element Analysis of RC Structures*, Willam K, Tanabe T (eds). ACI International, Farmington Hills, MI, 2001; ACI-SP-205-10:191–213.
27. Kwan WP, Billington SL. Unbonded posttensioned concrete bridge piers. II: seismic analyses. *Journal of Bridge Engineering* 2003; **8**:102–111.
28. Faria R, Oliver J, Cervera M. Modeling material failure in concrete structures under cyclic actions. *Journal of Structural Engineering* 2004; **130**(12):1997–2005.
29. Mirzabozorg H, Ghaemian M. Nonlinear behavior of mass concrete in 3d problems using a smeared crack approach. *Earthquake Engineering and Structural Dynamics* 2005; **34**:247–269.
30. Spiliopoulos KV, Lykidis GC. Three dimensional finite element analysis of reinforced concrete under dynamic loading. *European Congress on Computer Methods in Applied Sciences and Engineering, ECCOMAS 2004*. Jyväskylä, Finland, 24–28 July, 2004.
31. Kotsovos MD. Concrete. A brittle fracturing material. *RILEM Materials and Structures* 1984; **17**:107–115.
32. Kotsovos MD, Spiliopoulos KV. Modeling of crack closure for finite element analysis of structural concrete. *Computers and Structures* 1998; **69**:383–398.
33. Menegotto M, Pinto PE. Method of analysis for cyclically loaded reinforced concrete plane frames including changes in geometry and non elastic behaviour of elements under combined normal force and bending. *Proceedings of the IABSE Symposium on Resistance and Ultimate Deformability of Structures Acted on by Well Defined Repeated Loads*, Lisbon, 1973.
34. Elwi AE, Hrudey TM. Finite element model for curved embedded reinforcement. *Journal of Engineering Mechanics* 1989; **115**:740–754.
35. Barzegar F, Maddipudi S. Generating reinforcement in FE modelling of concrete structures. *Journal of Structural Engineering* 1994; **120**:1656–1662.
36. Gomes HM, Awruch AM. Some aspects on three-dimensional numerical modelling of reinforced concrete structures using the finite element method. *Advances in Engineering Software* 2001; **32**:257–277.
37. Hitchings D. *FE77 v. 2.56–User's and Programmer's Manual*. London, 2001.
38. Lefas ID, Kotsovos MD. Strength and deformation characteristics of reinforced concrete walls under load reversals. *ACI Structural Journal* 1990; **87**(6):716–726.
39. Chopra AK. *Dynamics of Structures—Theory and Applications to Earthquake Engineering*. Prentice-Hall: Englewood Cliffs, NJ, 2001.
40. Carydis PG. European Commission—Human Capital and Mobility Programme, Prenormative Research in Support of Eurocode 8, shaking Table Tests of Reinforced Concrete Frames. *Report No. 8*, 1997.